Journal of Civil Engineering Research 2017, 7(1): 17-33
DOI: 10.5923/j.jce.20170701.03

Isolation Performance Assessment of Adaptive Behaviour of Triple Friction Pendulum

Felix Weber[1,*], Johann Distl[2], Christian Braun[3]

[1]R&D Department of Maurer Söhne Engineering, Maurer Switzerland GmbH, Zurich, Switzerland
[2]R&D Department of Maurer Söhne Engineering, Maurer Söhne Engineering GmbH & Co. KG, Munich, Germany
[3]Executive Board of MAURER SE, MAURER SE, Munich, Germany

Abstract The triple friction pendulum is a promising approach towards isolators with adaptive behaviour. In general, its friction and stiffness properties depend on bearing displacement and sliding regime, respectively, whereby also its isolation performance in terms of absolute structural acceleration depends on sliding regime and consequently on peak ground acceleration of the considered accelerogram. This paper therefore investigates the isolation performance of the triple friction pendulum as function of various peak ground accelerations ranging from very small values up to the maximum value at which the full displacement capacity of the pendulum is used. The results are compared to those of the conventional double friction pendulum with same curvature and same displacement capacity. The comparative study shows that the triple friction pendulum a) performs better at small peak ground accelerations (<20% of its maximum) thanks to the low friction of the articulated slider assembly that triggers relative motion in the bearing even at very low shaking level, b) generates slightly worse isolation when sliding regimes II to IV are activated, and c) evokes a strongly deteriorated isolation when sliding regime V is triggered due to its increased stiffness and reduced friction properties. It is also found that the combination of increased stiffness and reduced friction cannot reduce the displacement capacity of the triple friction pendulum because the beneficial effect of increased stiffness is offset by the reduced friction of sliding regime V. The paper is closed by the numerical study of a pendulum whose friction coefficient is controlled in proportion to the bearing displacement amplitude. This promising approach can be seen as objective function for the future development of adaptive friction pendulums.

Keywords Damping, Earthquake, Friction, Isolation, Triple friction pendulum

1. Introduction

The base isolation of civil engineering structures is the common countermeasure against hazardous structural vibrations due to earthquake excitation [1-4]. Various types of elastomeric bearings and spherical friction pendulums (FP) belong to the class of passive isolators that exert the superposition of a stiffness force and damping force [5-11]. For minimum structural response the stiffness is designed to significantly increase the fundamental period of the isolated structure [12] with the constraint of the re-centring condition [13, 14] and the friction is tuned to add damping to the structure at isolation frequency [15, 16]. This design is made by the structural engineer for the given elastic response spectrum with associated ground acceleration [17] corresponding to the design basis earthquake (DBE) or the maximum considered earthquake (MCE). Due to the constant friction and stiffness parameters of non-adaptive FPs, these devices can only be optimally tuned to one of the aforementioned earthquake scenarios. This trade-off problem may be solved by the rather costly combination of lubricated spherical surfaces and external viscous dampers with properly tuned α exponent. Another but also expensive approach represent active, semi-active and hybrid isolation systems based on controlled hydraulic actuators [18], variable orifice dampers [19], variable stiffness devices [20, 21], shape memory alloys [22], electrorheological dampers [23] and magnetorheological dampers [24-26] due to their ability to emulate controllable stiffness and damping forces [27, 28].

The economic disadvantages of the above mentioned solutions triggered the development of so-called adaptive FPs which are purely passive devices but their stiffness and friction properties depend on the displacement amplitude at which the FP is operated. This can be achieved by different radii and/or friction coefficients of modified single and double FPs and triple FPs [29-40] of which especially the triple FP has attracted the attention of many researchers and engineers as these devices exhibit significant adaptability. A thorough description of the theoretical functioning of triple FPs for kinematic excitation can be found in [30, 31]. Based on this description the triple FP is modelled by a series arrangement of spring, Coulomb friction and gap elements.

* Corresponding author:
f.weber@maurer.eu (Felix Weber)
Published online at http://journal.sapub.org/jce

The experimental validation of this modelling approach is described in [32-35] and an improved modelling approach is presented in [36].

According to [15, 16, 31] the triple FP is conceptualized to produce low friction at high stiffness for small bearing motion amplitudes and peak ground acceleration (PGA) values, respectively, generate increasing friction at significantly reduced stiffness for medium bearing displacement amplitudes and PGA values, respectively, due to DBE, evoke further augmented friction at even lower stiffness for large bearing displacement amplitudes and PGA values, respectively, due to MCE, and exhibit stiffening behaviour for bearing displacement amplitudes and PGA values, respectively, resulting from earthquakes beyond MCE. This adaptive behaviour of the friction and stiffness properties implies that the isolation performance of the triple FP has to be assessed as function of various PGA values to ensure that the triple FP is operated within all its sliding regimes. A first approach towards this goal is presented in [41] where several earthquakes are scaled to two PGA values; however, the triggered sliding regimes are not given whereby the obtained isolation performance results are difficult to interpret.

This paper aims at filling this gap by the following consecutive steps:

1. Assessing the force displacement trajectories of the triple FP in terms of cycle energy equivalent friction and elastic energy equivalent stiffness coefficients [42] as function of bearing displacement amplitude,
2. Quantifying the isolation performance of the triple FP in terms of absolute acceleration and drift of the isolated structure as function of various PGA values ranging from 0.5 m/s^2 to the maximum value at which the full displacement capacity is used whereby the isolation performance is assessed as function of the bearing displacement and different sliding regimes, respectively, and
3. Finally, an adaptive FP based on controlled friction damping is presented as objective function for the future development of adaptive FPs.

The studies 1 and 2 are based on the triple FP as designed in [31, 32] in order to guarantee that the triple FP is designed according to the published design philosophy.

The structure of the paper is as follows: Section 2 describes the triple FP under consideration and the double FP that is used as non-adaptive benchmark. Section 3 derives the cycle energy equivalent friction and elastic energy equivalent stiffness coefficients of the triple FP for kinematic excitation of the bearing and for force excitation due to ground acceleration when the bearing is installed underneath the isolated structure. The isolation performances due to the triple FP for several PGA-scaled measured earthquake acceleration time histories are presented in section 4 and compared to the results obtained from the double FP. The potential of a pendulum with real-time controlled friction damping is described in section 5. Section 6 closes the paper by a summary and conclusions.

2. Friction Pendulums under Consideration

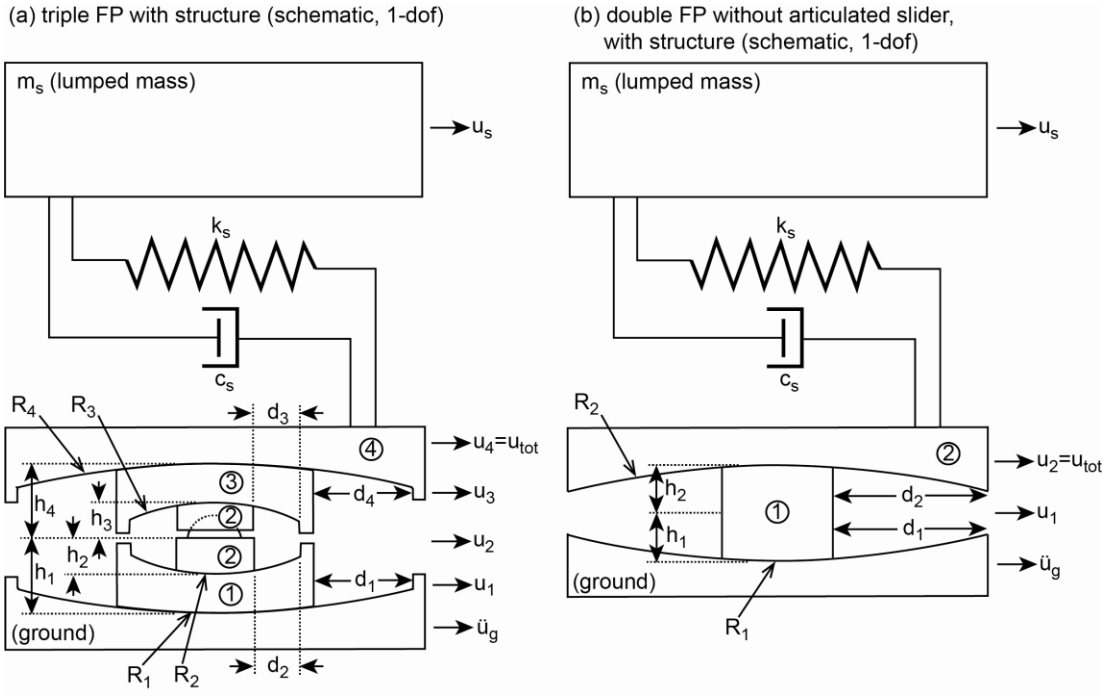

Figure 1. Sketches of (a) triple friction pendulum and (b) non-adaptive double friction pendulum with structure simplified as single degree-of-freedom system (1-dof)

2.1. Triple Friction Pendulum

The triple FP is composed of the two concave steel plates 0 and 4 and the articulated slider assembly in between with the rigid slider and the two concave slide plates 1 and 3 (Figure 1(a)). The surfaces of the slide plates 1 and 3 that are in contact with the concave steel plates 0 and 4 and both surfaces of the slider are coated with a non-metallic sliding material. The design parameters of triple FP are therefore:

- the four effective radii $R_{eff,i} = R_i - h_i$ where R_i and h_i, respectively, are the geometric radius of surface i and the radial distance of surface i to the pivot point of the articulated slider, respectively,
- the four friction coefficients μ_i, and
- the four displacement capacities d_i.

The associated four relative motions are u_1 of plate 1 relative to plate 0, $u_2 - u_1$ of the slider relative to plate 1, $u_3 - u_2$ of plate 3 relative to the slider and $u_4 - u_3$ of plate 4 relative to plate 3 whereby the total bearing displacement becomes $u_{tot} = u_4$.

The vertical load $W = g\,m_s$ (g: acceleration of gravity, m_s: structural mass) on the bearing is assumed to be constant and uniformly distributed on concave plate 4 to guarantee proper functioning of the kinematics of the triple FP. The variations of the vertical load due to the small vertical acceleration of the building when the slider moves towards one side of the bearing are neglected as the focus of the study under consideration is the isolation assessment of the isolator in horizontal direction.

The usual design of the triple FP according to [31, 32] is given by $R_{eff,1} = R_{eff,4} >> R_{eff,2} = R_{eff,3}$ and $\mu_2 = \mu_3 < \mu_1 < \mu_4$ in order to ensure that relative motion initiates on surfaces 2 and 3 with low friction which is followed by increasing friction characteristics when sliding also occurs on surfaces 1 and 4 and is finalized by a stiffening effect at reduced friction when concave slide plates 1 and 3 contact the restrainers of concave plates 0 and 4 whereby only the articulated slider assembly works. This behaviour is achieved when the design of the triple FP satisfies the conditions $d_2 > (\mu_1 - \mu_2) R_{eff,2}$, $d_3 > (\mu_4 - \mu_3) R_{eff,3}$ and $d_1 > (\mu_4 - \mu_1) R_{eff,1}$.

2.2. Properties of Triple Friction Pendulum

The aim of the present study is to assess the isolation performance of the triple FP as it is originally designed and published in the literature [31, 32]; the friction coefficients used in the present study represent the average values of the identified values given in [32]. This triple FP represents a mock-up triple FP whereby the effective radii 1 and 4 and consequently the isolation time period are rather small. In order to guarantee a fair comparison with the non-adaptive double FP, the effective radii 1 and 2 of the double FP and consequently its isolation time period are equal those of the triple FP. Table 1 shows the relevant parameters including the total displacement capacity $d_{tot} = d_1 + d_2 + d_3 + d_4$ (without the small influence of rotation). The vertical load W =112 kN on the bearing due to the structure also corresponds to that given in [32] that leads to a surface pressure of 54.83 MPa on the slider which represents a common value.

Table 1. Properties of Triple and Double Friction Pendulums

Triple FP	Double FP
$R_{eff,1} = R_{eff,4} = 0.435$ m $R_{eff,2} = R_{eff,3} = 0.053$ m	$R_{eff,1} = R_{eff,2} = 0.435$ m
$\mu_1 = 3.1\%$ $\mu_2 = \mu_3 = 1.75\%$ $\mu_4 = 11.4\%$	$\mu_1 = \mu_2$ (reasonable value)
$d_1 = d_4 = 0.064$ m $d_2 = d_3 = 0.019$ m $d_{tot} = 0.166$ m	$d_1 = d_2 = 0.083$ m $d_{tot} = 0.166$ m
$R_1 = R_4 = 0.473$ m $R_2 = R_3 = 0.076$ m $h_1 = h_4 = 0.038$ m $h_2 = h_3 = 0.023$ m	$R_1 = R_2 = 0.473$ m $h_1 = h_2 = 0.038$ m

2.3. Non-Adaptive Double Friction Pendulum

The non-adaptive double FP consists of two concave steel plates and the rigid slider in between which is coated with a non-metallic sliding material (Figure 1(b)). The motion of the slider relative to the plate 0 is denoted as u_1 and between plate 2 and slider is $u_2 - u_1$ whereby the total bearing motion becomes $u_{tot} = u_2$ (without small influence of rotation). In order to secure a fair comparison of the isolation performances resulting from the triple and double FPs, the isolation frequency of the double FP is selected to be equal the lower isolation frequency of the triple FP. Hence, the effective radii of the double FP $R_{eff,1}$ and $R_{eff,2}$ are equal the effective radii of the two concave plates 0 and 4 of the triple FP (Table 1). Furthermore, total bearing displacement $d_{tot} = d_1 + d_2$ of the double FP is equal to d_{tot} of the triple FP to guarantee equal displacement capacities. The friction coefficients of the double FP are assumed to be equal, i.e. $\mu_1 = \mu_2$, whereby the results due to the double FP are also valid for a single FP with double effective radius.

3. Equivalent Friction and Stiffness Coefficients

3.1. Kinematic Excitation

3.1.1. Force Displacement Trajectories

The horizontal bearing force f_H of the triple FP is the sum of the forces due to friction, effective radius and restrainer deformation. This force resulting from kinematic excitation at the fundamental frequency of the structure fr_s is calculated adopting the formulas for all five sliding regimes as described in [31]. The computation of f_H is not only made for the maximum displacement amplitudes $U_{tot,j}$ ($j = 1,...,5$) of the five sliding regimes but for various total amplitudes U_{tot} with $min(U_{tot})$ =1 mm, increment ≤ 2 mm and $max(U_{tot}) = U_{tot,5}$. The force displacement trajectories resulting from the maximum displacement amplitudes $U_{tot,i}$ of sliding regime i are depicted in Figures 2(a-e) by the thick lines in grey; the thin dashed lines in red, green and blue represent the force displacement trajectories due to three selected U_{tot} that are smaller than $U_{tot,j}$ of the corresponding sliding regime. For the sake of completeness, the force displacement trajectory for 0.5 mm restrainer deformation, i.e. $U_{tot} = U_{tot,5} + 0.5$ mm, is also shown (Figure 2(f)). Notice that the force displacement trajectories plotted in Figure 2 slightly differ from those depicted in figure 4 of [32] because the force displacement trajectories shown figure 4 of [32] are computed with μ_1, μ_2, μ_3 and μ_4 identified for each sliding regime itself which yields different μ_1, μ_2, μ_3 and μ_4 for the five ($j = 1,...,5$) sliding regimes. It is also underlined that the force displacement trajectories depicted in Figure 2 differ from those shown in [31] because the force displacement trajectories of [31] are computed for $R_{eff,1} \neq R_{eff,4}$ and $R_{eff,2} \neq R_{eff,3}$.

3.1.2. Equivalent Friction and Stiffness Coefficients

From the force displacement trajectories resulting from all considered U_{tot} ($min(U_{tot})$ =1 mm, increment ≤2 mm, $max(U_{tot}) = U_{tot,5}$) the equivalent friction coefficient μ_{equiv} is numerically computed from the cycle energy of f_H [27, 42]

$$\mu_{equiv} = \frac{1}{4 W U_{tot}} \int_0^{1/fr} f_H \, \dot{u}_{tot} \, dt \qquad (1)$$

where fr denotes the frequency of u_{tot} and $\dot{u}_{tot}$ is the total bearing velocity; the equivalent stiffness coefficient k_{equiv} is numerically derived from the elastic energy of f_H [27, 42]

$$k_{equiv} = \frac{1}{U_{tot}^2} \left\{ \int_0^{U_{tot}} f_H \, du_{tot} + \int_{U_{tot}}^{0} f_H \, du_{tot} \right\} \qquad (2)$$

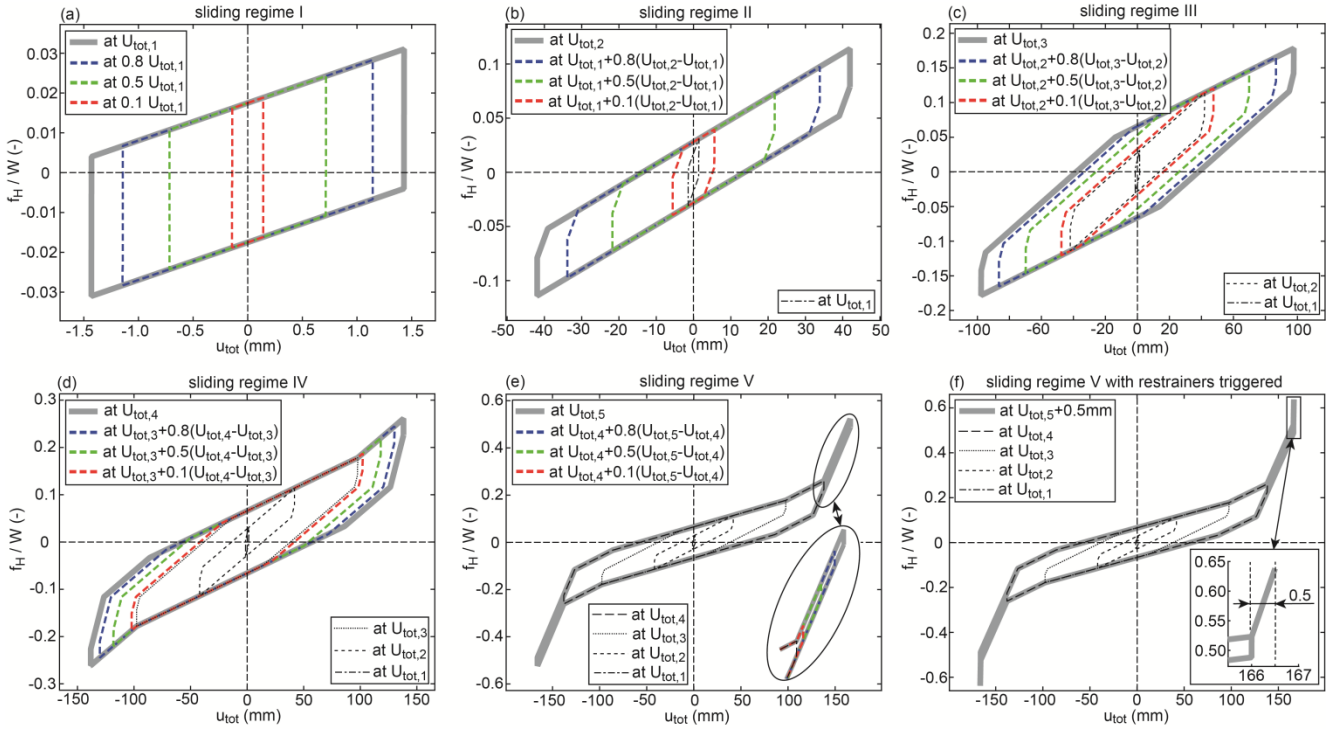

Figure 2. Force displacement trajectories resulting from kinematic excitation

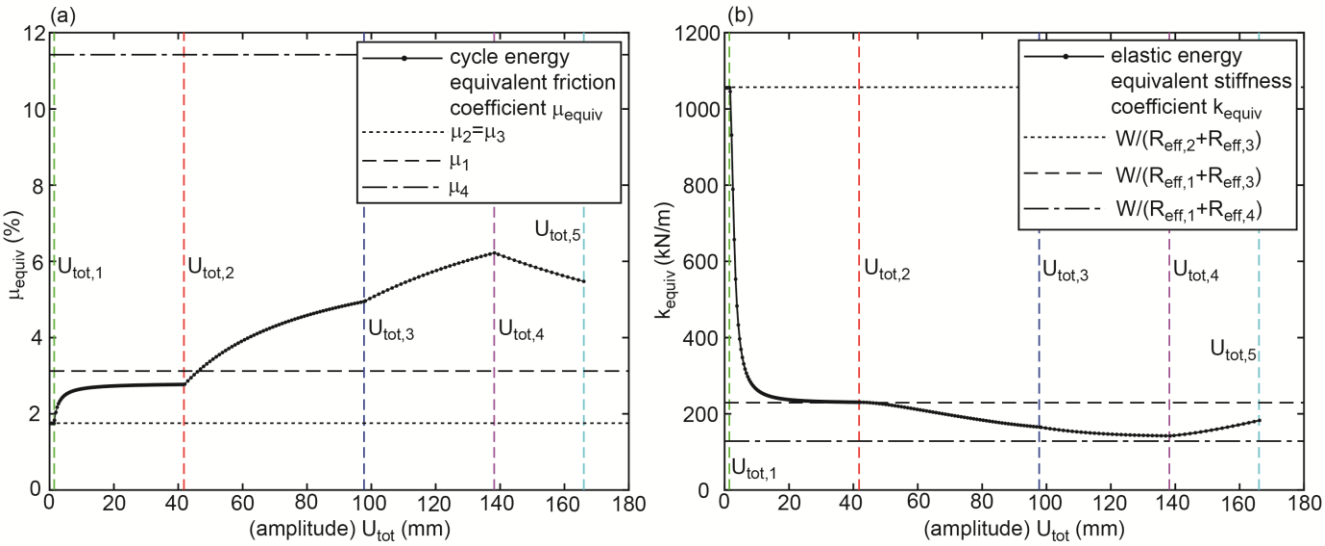

Figure 3. (a) Cycle energy equivalent friction coefficient and (b) elastic energy equivalent stiffness coefficient as function of total displacement amplitude identified from kinematic excitation

3.1.3. Discussion

The obtained energy equivalent coefficients are plotted in Figures 3(a, b) versus the total amplitudes U_{tot} of all computed force displacement trajectories. The following observations can be made (readers are referred to [31] for detailed description of the sliding regimes of the triple FP):

- Sliding regime I: relative motion only occurs on sliding surfaces 2 and 3 with equal radii and friction coefficients (Figure 2(a)) [31]. This explains the findings $\mu_{equiv} = \mu_2 = \mu_3$, $k_{equiv} = W / R_{eff,2} = W / R_{eff,3}$.
- Sliding regime II: relative motion occurs on surfaces 1, 2 and 3 (Figure 2(b)) [31]. The resulting μ_{equiv} which can be interpreted as an "average" friction coefficient is therefore greater than $\mu_2 = \mu_3$ but smaller than μ_1 while k_{equiv} is dominated by $W / R_{eff,1}$ due to $R_{eff,1} >> R_{eff,2} = R_{eff,3}$.
- Sliding regime III: besides sliding on surfaces 1, 2 and 3 sliding is also triggered on surface 4 [31]. The resulting force displacement trajectory is dominated by simultaneous sliding on surfaces 1, 2 and 3 with slope $(R_{eff,1} + R_{eff,2} + R_{eff,3})^{-1}$ and all surfaces 1 to 4 with slope $(R_{eff,1} + R_{eff,2} + R_{eff,3} + R_{eff,4})^{-1}$ (Figure 2(c)). μ_{equiv} turns out to be significantly smaller than μ_4 because the entire sliding motion is split into simultaneous sliding on surfaces 1, 2 and 3 and simultaneous sliding on all surfaces 1 to 4. Therefore k_{equiv} is between $W / (R_{eff,1} + R_{eff,2} + R_{eff,3})$ and $W / (R_{eff,1} + R_{eff,2} + R_{eff,3} + R_{eff,4})$.
- Sliding regime IV: sliding on surface 1 is stopped by its restrainer which evokes a stiffening effect in the force displacement trajectory for $|u_{tot}| > U_{tot,3}$ (Figure 2(d)) whereby the decreasing trend of k_{equiv} levels off (Figure 3(b)) [31]. Since simultaneous sliding on surfaces 1 and 4 dominates the force displacement trajectory of sliding regime IV (Figure 2(d)), μ_{equiv} increases within sliding regime IV towards μ_4 but is significantly smaller than μ_4 because of $\mu_1 < \mu_4$ (Figure 3(a)).
- Sliding regime V: sliding on surfaces 1 and 4 are stopped by their restrainers while sliding continuous on sliding surfaces 2 and 3. This evokes the stiffening behaviour at very small friction for $|u_{tot}| > U_{tot,4}$ (Figure 2(e)). As a result, k_{equiv} increases while μ_{equiv} decreases in sliding regime V.

3.2. Force Excitation

In order to compute the energy equivalent friction and stiffness coefficients for force excitation, first, the coupled equations of motion of the isolated structure and all bearing plates of the triple FP for ground acceleration input are derived (section 3.2.1), then the input acceleration is described (section 3.2.2) and, finally, the obtained results are discussed (section 3.2.3).

3.2.1. Coupled Non-Linear Equations of Motion

The equation of motion of the structure with ground acceleration $\ddot{u}_g$ as excitation input becomes

$$m_s \ddot{u}_s + c_s (\dot{u}_s - \dot{u}_4) + k_s (u_s - u_4) = -m_s \ddot{u}_g \quad (3)$$

where $\ddot{u}_s$ denotes the relative structural acceleration,

$m_s = W / g$ is the modal mass (g acceleration of gravity), $c_s = 2\zeta_s \sqrt{k_s\, m_s}$ is the viscous damping coefficient with damping ratio ζ_s=1%, k_s is the stiffness coefficient, and $u_s - u_4$ and $\dot{u}_s - \dot{u}_4$, respectively, represent the relative displacement and relative velocity, respectively, between the structure and concave plate 4 of the triple FP (Figure 1(a)). The excitation force due to the ground acceleration $\ddot{u}_g$ is given by the d'Alembert term $-m_s \ddot{u}_g$ on the right side of (3) whereby the total acceleration of the structure becomes $\ddot{u}_s + \ddot{u}_g$. The structural stiffness $k_s = (2\pi\, fr_s)^2 m_s$ is selected such that the fundamental frequency fr_s of the non-isolated structure is two times higher than the lower isolation frequency of the triple FP

$$fr_{isolation} = \frac{1}{2\pi}\sqrt{\frac{g}{R_{eff,1} + R_{eff,4}}} \tag{4}$$

$$fr_s = 2\, fr_{isolation} \tag{5}$$

Equation (4) yields fr_s =1.069 Hz representing a typical value of non-isolated structures that require base isolation. All relevant structural properties are given in Table 2 where the given mass corresponds to the mass of the structure supported by one pendulum.

Table 2. Structural properties

m_s (kg)	fr_s (Hz)	ζ_s (%)
11417	1.069	1.0

The formulation of the equation of motion for concave plate 4 with mass m_4 yields (Figure 1(a))

$$\begin{aligned} &m_4\,\ddot{u}_4 + f_{h,4} + \frac{W}{R_{eff,4}}(u_4 - u_3) + f_{r,4} = \dots \\ &c_s(\dot{u}_s - \dot{u}_4) + k_s(u_s - u_4) - m_4\,\ddot{u}_g \end{aligned} \tag{6}$$

where $\ddot{u}_4$ denotes the relative acceleration of m_4, $f_{h,4}$ represents the friction force of surface 4, $W / R_{eff,4}$ is the stiffness due to the effective radius of concave plate 4 and $f_{r,4}$ is the restrainer force of concave plate 4. $f_{h,4}$ is modelled by the hysteretic friction force model where the pre-sliding regime is modelled by a stiffness force [43, 44]

$$f_{h,4} = \begin{cases} k_{h,4}(u_4 - u_3) & : \quad pre-sliding \\ \mu_4 W\, sgn(\dot{u}_4 - \dot{u}_3) & : \quad sliding \end{cases} \tag{7}$$

The pre-sliding stiffness $k_{h,4}$ is selected to be 5e2 times greater than the stiffness due to the effective radius, i.e. $k_{h,4} = 5e2W / R_{eff,4}$, sgn represents the signum function and $\dot{u}_4 - \dot{u}_3$ is the relative velocity between the plates 4 and 3. The force of the restrainer is modelled as a linear stiffness force that is only triggered when plate 3 is in contact with the restrainer of plate 4

$$f_{r,4} = \dots \begin{cases} k_{r,4}\left(|u_4 - u_3| - d_4\right) sgn(u_4 - u_3) : |u_4 - u_3| \geq d_4 \\ 0 : |u_4 - u_3| < d_4 \end{cases} \tag{8}$$

where the restrainer stiffness $k_{r,4}$ is selected to be 1e2 times greater than $W / R_{eff,4}$. For the concave slide plate 3 with mass m_3, the equation of motion is

$$\begin{aligned} &m_3\,\ddot{u}_3 + f_{h,3} + \frac{W}{R_{eff,3}}(u_3 - u_2) + f_{r,3} = \dots \\ &f_{h,4} + \frac{W}{R_{eff,4}}(u_4 - u_3) + f_{r,4} - m_3\,\ddot{u}_g \end{aligned} \tag{9}$$

where $\ddot{u}_3$ is the relative acceleration of m_3 and $f_{h,3}$ and $f_{r,3}$, respectively, represent the hysteretic friction force and restrainer force, respectively, that are formulated analogically with equations (7, 8). The equation of motion for the slider mass m_2 has the same form as for m_3

$$\begin{aligned} &m_2\,\ddot{u}_2 + f_{h,2} + \frac{W}{R_{eff,2}}(u_2 - u_1) + f_{r,2} = \dots \\ &f_{h,3} + \frac{W}{R_{eff,3}}(u_3 - u_2) + f_{r,3} - m_2\,\ddot{u}_g \end{aligned} \tag{10}$$

where $\ddot{u}_2$ denotes the relative acceleration of the slider and $f_{h,2}$ and $f_{r,2}$, respectively, are given analogically with equations (7, 8). The equation of motion of concave plate 1 with mass m_1 and relative acceleration $\ddot{u}_1$ becomes

$$\begin{aligned} &m_1\,\ddot{u}_1 + f_{h,1} + \frac{W}{R_{eff,1}}u_1 + f_{r,1} = \dots \\ &f_{h,2} + \frac{W}{R_{eff,2}}(u_2 - u_1) + f_{r,2} - m_1\,\ddot{u}_g \end{aligned} \tag{11}$$

where $f_{h,1}$ and $f_{r,1}$, respectively, are given as follows

$$f_{h,1} = \begin{cases} k_{h,1}\,u_1 & : \quad pre-sliding \\ \mu_1 W\, sgn(\dot{u}_1) & : \quad sliding \end{cases} \tag{12}$$

$$f_{r,1} = \begin{cases} k_{r,1}\left(|u_1| - d_1\right) sgn(u_1) & : \quad |u_1| \geq d_1 \\ 0 & : \quad |u_1| < d_1 \end{cases} \tag{13}$$

because u_1 is the displacement of plate 1 relative to plate 0 (Figure 1(a)). It must be added that $k_{h,1} = k_{h,2} = k_{h,3} = k_{h,4}$ and $k_{r,1} = k_{r,2} = k_{r,3} = k_{r,4}$ are assumed and that the values of m_1, m_2, m_3 and m_4

are calculated based on the geometrical data given in [32] assuming steel as material.

3.2.2. Dynamic Simulation

The coupled non-linear differential equations of motion are solved in the time domain in Matlab/Simulink® using the solver ode15s(stiff/NDF) with maximum relative tolerance of 1e-3 and variable step size with upper bound of 1e-5 s.

3.2.3. Ground Acceleration

In order to trigger all sliding regimes of the triple FP under force excitation step by step, the ground acceleration is assumed to be a sinusoidal function with linearly increasing amplitude and frequency fr_s (Figure 4(a)). The resulting relative displacements show that the restrainer of plate 0 is first triggered, then the restrainers of plate 0 and 4 are triggered during one cycle of vibration and finally all four restrainers of plates 0, 1, 3 and 4 are triggered during one cycle of vibration (Figure 4(b)). Then, the simulation is stopped because the full displacement capacity of the bearing is depleted.

3.2.4. Discussion

The horizontal forces f_H of masses 1, 2, 3, 4 and the visco-elastic structural force are equal at every time instant t

$$\begin{aligned} &f_H(t) = ... \\ &f_{h,1}(t) + \frac{W}{R_{eff,1}} u_1(t) + f_{r,1}(t) = ... \\ &f_{h,2}(t) + \frac{W}{R_{eff,2}} \left(u_2(t) - u_1(t)\right) + f_{r,2}(t) = ... \\ &f_{h,3}(t) + \frac{W}{R_{eff,3}} \left(u_3(t) - u_2(t)\right) + f_{r,3}(t) = ... \\ &f_{h,4}(t) + \frac{W}{R_{eff,4}} \left(u_4(t) - u_3(t)\right) + f_{r,4}(t) = ... \\ &f_s(t) = ... \\ &c_s\left(\dot{u}_s(t) - \dot{u}_4(t)\right) + k_s\left(u_s(t) - u_4(t)\right) \end{aligned} \quad (14)$$

The corresponding force displacement trajectories are not congruent, see Figure 5(a), because of the different relative displacements u_1, $u_2 - u_1$, $u_3 - u_2$, $u_4 - u_3$ and $u_s - u_4$ (see also Figure 4(b)). Figure 5(b) plots f_H versus the total bearing displacement which can be compared with the force displacement trajectories from kinematic excitation (Figure 2). The main difference observed is that when sliding is also triggered on surface 4 (t >5.8 s, see Figure 4(b)), simultaneous sliding takes place on all four sliding surfaces which is confirmed by the slope of the force displacement trajectory (normalized by W) of $(R_{eff,1} + R_{eff,2} + R_{eff,3} + R_{eff,4})^{-1}$.

This observation reveals that the triple FP installed between foundation and structure and excited by ground acceleration behaves different than for kinematic excitation as described in [31]. In order to double-check this finding, half a cycle from sliding start to sliding stop is investigated in detail. Figure 6(a) depicts the four relative bearing displacements as function of time that are normalized when sliding initiates on surfaces 2 and 3. The corresponding force displacement trajectories of the same time interval are plotted in Figure 6(b). When sliding only occurs on surfaces 2 and 3, their horizontal forces are balanced by the pre-sliding stiffness forces $k_{h,1} u_1(t)$ and $k_{h,4}\left(u_4(t) - u_3(t)\right)$, respectively, of surfaces 1 and 4, respectively. Sliding on surface 1 initiates when the relative motions $u_2(t) - u_1(t)$ and $u_3(t) - u_2(t)$, respectively, are that large that the sum of increased stiffness forces due to the effective radii of surfaces 2 and 3 and the constant friction force balance the friction force of surface 1, that is

$$\begin{aligned} &\frac{W}{R_{eff,k}}\left(u_k(t) - u_{k-1}(t)\right) + ... \\ &\mu_k W\, sgn(\dot{u}_k(t) - \dot{u}_{k-1}(t)) = \mu_1 W\, sgn(\dot{u}_1(t)) \end{aligned} \quad (15)$$

where k =2 for the slider and k =3 for concave plate 3, which is highlighted by the circle symbol in Figures 6(a, b). With further increased relative motions $u_1(t)$, $u_2(t) - u_1(t)$ and $u_3(t) - u_2(t)$, respectively, the friction force $\mu_4 W\, sgn(\dot{u}_4(t) - \dot{u}_3(t))$ is balanced by the sum of the stiffness force due to $R_{eff,k}$ and friction force of surface k ($k = 1,...,3$) whereby sliding starts on surface 4 (diamond symbol in Figures 6(a, b)). All relative motions stop at the same time instant when all four hysteretic friction forces get back into their pre-sliding regimes (star symbol in Figures 6(a, b)).

Comparing the equivalent friction and stiffness coefficients due to forced excitation (Figures 7(a, b)) with those resulting from kinematic excitation (Figures 3(a, b)) shows:

- $U_{tot,j}$: The total displacement amplitudes of sliding regimes I to V are shifted to greater values; notice that $U_{tot,j}$ for the computation of the force displacement trajectories due to kinematic excitation (section 3.1) correspond to those given in [31].
- μ_{equiv}: The values of μ_{equiv} are almost the same as resulting from the force displacement trajectories due to kinematic excitation but are shifted to larger U_{tot} for the reason mentioned above and also significantly decreases when sliding regime V is activated.
- k_{equiv}: The softening effect of k_{equiv} is slightly bigger due to the simultaneous sliding on all four surfaces whereby $min(k_{equiv})$ gets close to $W/(R_{eff,1} + R_{eff,2} + R_{eff,3} + R_{eff,4})$ and the

stiffening effect due to sliding regime V is less pronounced.

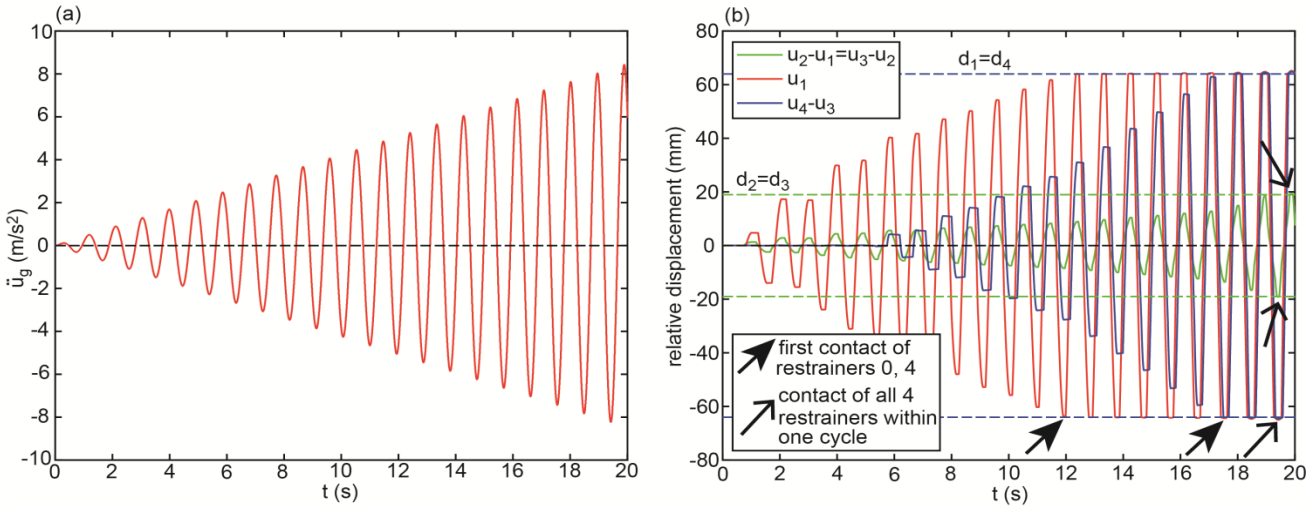

Figure 4. Behaviour of triple FP under force excitation: (a) introduced ground acceleration, (b) relative bearing displacements

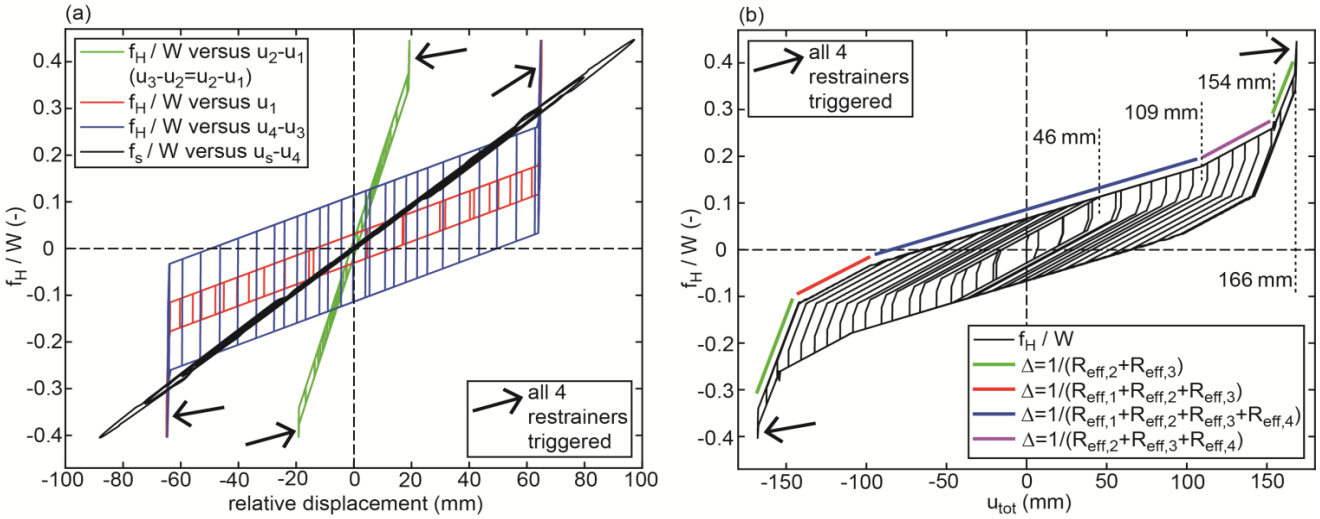

Figure 5. Behaviour of triple FP under force excitation: (a) horizontal force versus relative displacements of triple FP and primary structure, (b) horizontal force versus total displacement

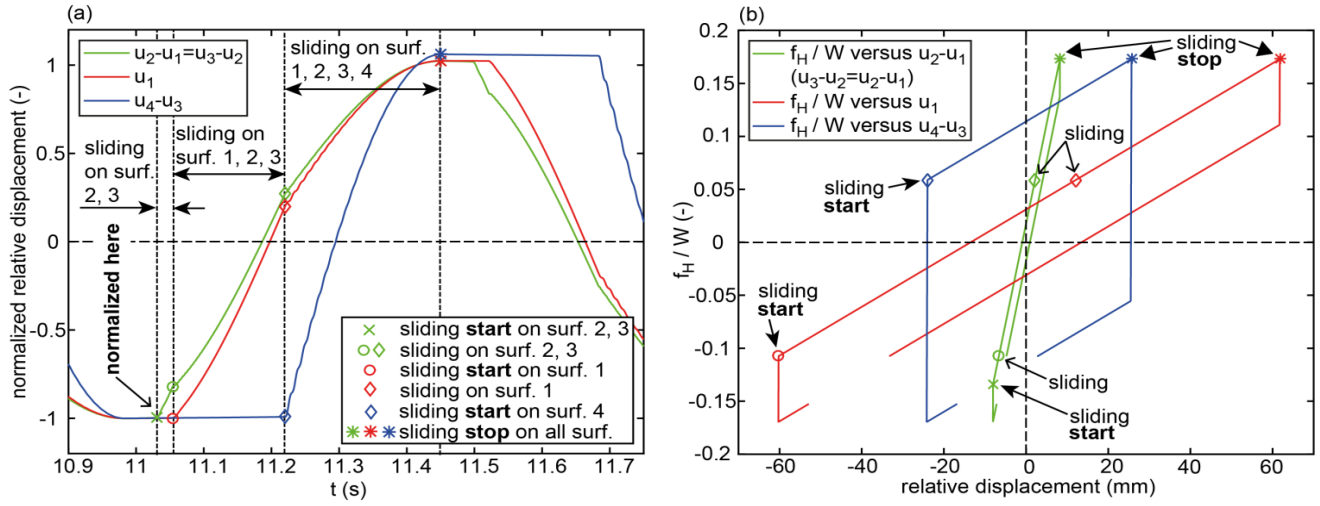

Figure 6. Simultaneous sliding on surfaces 1, 2, 3 and 4: (a) relative displacements as function of time and (b) horizontal force versus relative displacements

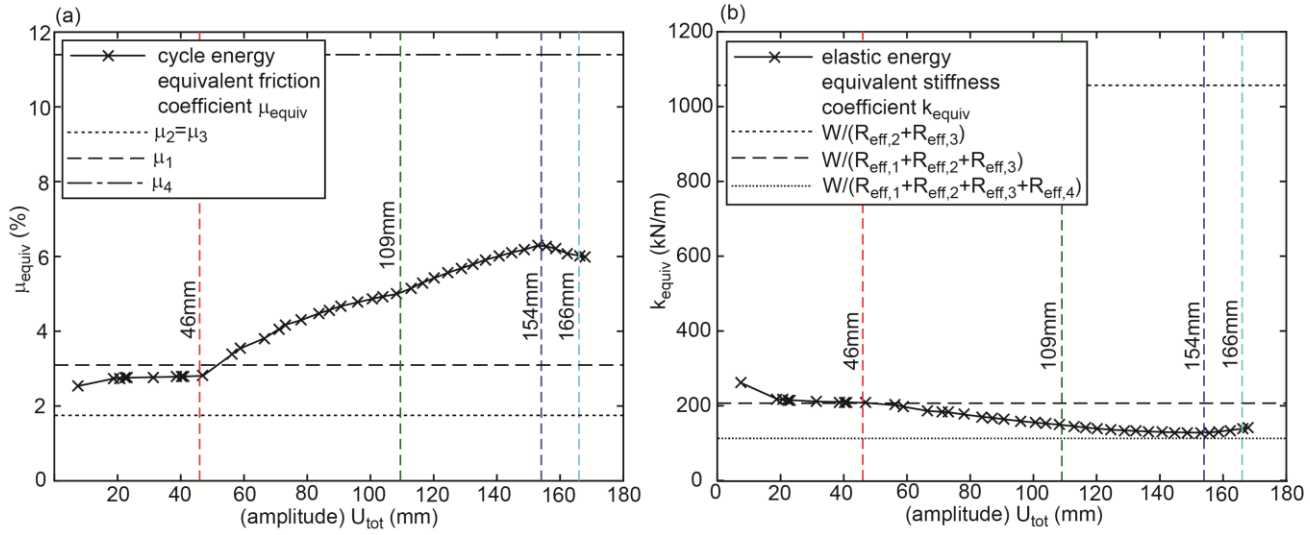

Figure 7. (a) Cycle energy equivalent friction coefficient and (b) elastic energy equivalent stiffness coefficient depending on total displacement amplitude and due to force excitation

4. Isolation Performance

Section 4 compares the isolation performance of the triple FP with that of the non-adaptive double FP with equal radii and equal friction coefficients. To guarantee a fair comparison the effective radii of the double FP are equal those of concave plates 0 and 4 of the triple FP (Table 1). Since the equivalent friction and stiffness coefficients of the triple FP depend on the bearing displacement amplitude, the isolation performance of the triple FP is assessed for various PGA values of several earthquakes to operate the triple FP within all its sliding regimes (section 4.1). The equal friction coefficients of the double FP are selected so that the restrainer deformation of the double FP at maximum PGA value is approx. equal that of the triple FP at maximum PGA value (section 4.2). The simulations are evaluated in terms of extremes of absolute acceleration and drift of the structure (section 4.3) and discussed in section 4.4.

4.1. PGA-scaled Ground Acceleration Time Histories

The simulations are performed with the ground acceleration time histories of the El Centro North-South (NS) earthquake, the El Centro East-West (EW) earthquake, the Loma Prieta earthquake, the Kobe earthquake and the Northridge earthquake. In order to operate the triple FP within all its sliding regimes the ground acceleration time histories are scaled by the following PGA-values in m/s^2

$$PGA = [\,0.5,1,2,...,PGA_{max}\,] \tag{16}$$

where the maximum PGA value PGA_{max} is chosen so that the maximum restrainer deformation of the triple FP is less than 1 mm. Due to the different frequency contents of the considered earth-quakes PGA_{max} becomes 7.8 m/s^2 for the El Centro NS earthquake, 4.9 m/s^2 for the El Centro EW earthquake, 3.2 m/s^2 for the Loma Prieta earthquake, 3.82 m/s^2 for the Kobe earthquake and 6.45 m/s^2 for the Northridge earthquake.

4.2. Friction Coefficient of Double Friction Pendulum

The friction coefficients $\mu_1 = \mu_2$ of the double FP are selected so that the restrainer deformation of the double FP is less than 1 mm at PGA_{max}. This ensures that displacement capacities of both the double and triple FPs are fully depleted at PGA_{max}. The resulting friction coefficients are $\mu_1 = \mu_2 =$ 6.0% for the El Centro NS earthquake, $\mu_1 = \mu_2 =$ 6.5% for the El Centro EW earthquake, $\mu_1 = \mu_2 =$ 4.5% for the Loma Prieta earthquake, $\mu_1 = \mu_2 =$ 5.5% for the Kobe earthquake and $\mu_1 = \mu_2 =$ 4.5% for the Northridge earthquake. In addition, all simulations are also performed with $\mu_1 = \mu_2 =$ 6.5% assuming a double FP with one friction coefficient.

4.3. Evaluation Criteria

The isolation performance is assessed by the commonly adopted two criteria [24, 26]:

- extreme of the absolute structural acceleration $max\left(\left|\ddot{u}_s + \ddot{u}_g\right|\right)$, and
- extreme of the structural drift $max\left(\left|u_s - u_{tot}\right|\right)$ where $u_{tot} = u_4$ for the triple FP and $u_{tot} = u_2$ in case of the double FP (Figures 1(a, b)).

4.4. Results

4.4.1. Simulation Tool

For the simulations of the structure with triple FP the coupled non-linear differential equations de-scribed in

section 3.2.1 are solved in Matlab/Simulink® (solver ode15s(stiff/NDF), maximum relative tolerance 1e-3, variable step size with upper bound of 1e-5 s) for the PGA-scaled ground accelerations of the five considered earthquakes. For the simulations of the structure with double FP, the equations of motion are reformulated for the two degrees of freedom u_1 and $u_2 - u_1$ of the double FP.

4.4.2. Absolute Acceleration and Drift of Structure

The simulation result of $max(|\ddot{u}_s + \ddot{u}_g|)$ and $max(|u_s - u_{tot}|)$ for the El Centro NS earthquake are depicted in Figures 8(a, b). It is observed that $max(|\ddot{u}_s + \ddot{u}_g|)$ and $max(|u_s - u_{tot}|)$ show the same trend as function of PGA which also applies to the simulation results of the other four earthquakes. This is explained by the fact that the structure is modelled as a single degree-of-freedom system which is the common approach when the isolation frequency is significantly below the natural frequency of the structure [45, 46] (Fig. 1). Therefore, Figures 9(a, b) and 10(a, b) only depict $max(|\ddot{u}_s + \ddot{u}_g|)$ resulting from the simulations of the El Centro EW, the Loma Prieta, the Kobe and the Northridge earthquake.

4.4.3. Triple Friction Pendulum Compared with Double Friction Pendulum

The numerical results of all considered earthquakes and PGA values reveal:

- The triple FP performs better at small the PGA values: PGA<2.2 m/s^2 for the El Centro NS, PGA<1.46 m/s^2 for El Centro EW, PGA<0.85 m/s^2 (<1.12 m/s^2 for $\mu_1 = \mu_2 = 6.5\%$) for the Loma Prieta, PGA<0.59 m/s^2 (<0.63 m/s^2 for $\mu_1 = \mu_2 = 6.5\%$) for the Kobe and PGA<1.12 m/s^2 (<1.83 m/s^2 for $\mu_1 = \mu_2 = 6.5\%$) for the Northridge earthquake.
- The double FP outperforms the triple FP for PGA values greater than the values given above.
- The isolation performances of both FPs at PGA_{max} are almost equal because PGA_{max} triggers approx. the same restrainer deformation (see section 4.1).
- The double FP with 6.5% friction (plotted in green) performs best because the higher friction reduces the bearing relative motion whereby restrainers are not triggered at $PGA = PGA_{max}$.

4.4.4. Triple Friction Pendulum with Different Friction Coefficients

The fact that the double FPs perform significantly better for most PGA values than the triple FP with $\mu_1 = 3.1\%$ and $\mu_4 = 11.4\%$ may be caused by suboptimal tunings of μ_1 and μ_4 of the triple FP; notice that $\mu_1 = 3.1\%$ and $\mu_4 = 11.4\%$ represent the experimentally identified mean values presented in [32]. Since the good results of the double FPs for the El Centro NS earthquake are obtained with significantly greater friction coefficients than 3.1%, two other triple FPs with increased friction coefficients, i.e. $\mu_1 = 4\%$ and $\mu_4 = 13\%$ and $\mu_1 = 5\%$ and $\mu_4 = 15\%$, are also computed. The results, which are included in Figures 8(a, b), demonstrate that increased friction coefficients μ_1 and μ_4 do hardly improve the isolation performance of the triple FP for most PGA values except in the vicinity of PGA_{max} due to the greater friction coefficients that reduce the total bearing motion whereby the restrainer deformation becomes smaller in case of μ_1 =4% and μ_4 =13% and becomes zero for μ_1 =5% and μ_4 =15%. It should be added that increased friction coefficients in case of the double FP would also avoid the activation of the restrainers whereby also the isolation results of the double FP at PGA values close to PGA_{max} would be improved.

4.4.5. Impact of Sliding Regime V

The results depicted in Figures 8(a, b)-10(a, b) clearly point out that the isolation performance of the triple FP deteriorates in the vicinity of PGA_{max}. The double-check of all force displacement trajectories of all simulations reveals that this coincides with the activation of sliding regime V (Figures 11(a, b, c)) that is characterized by significantly increased stiffness and significantly reduced friction. The combination of increased stiffness and reduced friction:

1. evokes the deterioration of the isolation because increased stiffness is equivalent to reduced isolation time period which would require increased friction to compensate for the isolation deterioration, and
2. cannot reduce the bearing displacement capacity demand since the stiffening behaviour is offset by the reduced friction which is confirmed by the equal restrainer deformations at PGA_{max} of the triple and double FPs with equal to d_{tot} (Figures 11(d, e, f)).

In contrast to sliding regime V sliding regime IV does not lead to a deterioration of the isolation performance despite the small stiffening effect of sliding regime IV as observed in Figure 12(a) because the activation of sliding regime generates a further increase of the equivalent friction coefficient as depicted in Figures 3(a) and 7(a). Figures 12(b-f) show that the force displacement trajectories of the triple FP at medium to small PGA values is dominated by sliding regimes II and III while sliding regime I is only relevant at PGA=0.5 m/s^2 which is also seen from the values of μ_{equiv} and k_{equiv} in Figures 3(a, b) and 7(a, b).

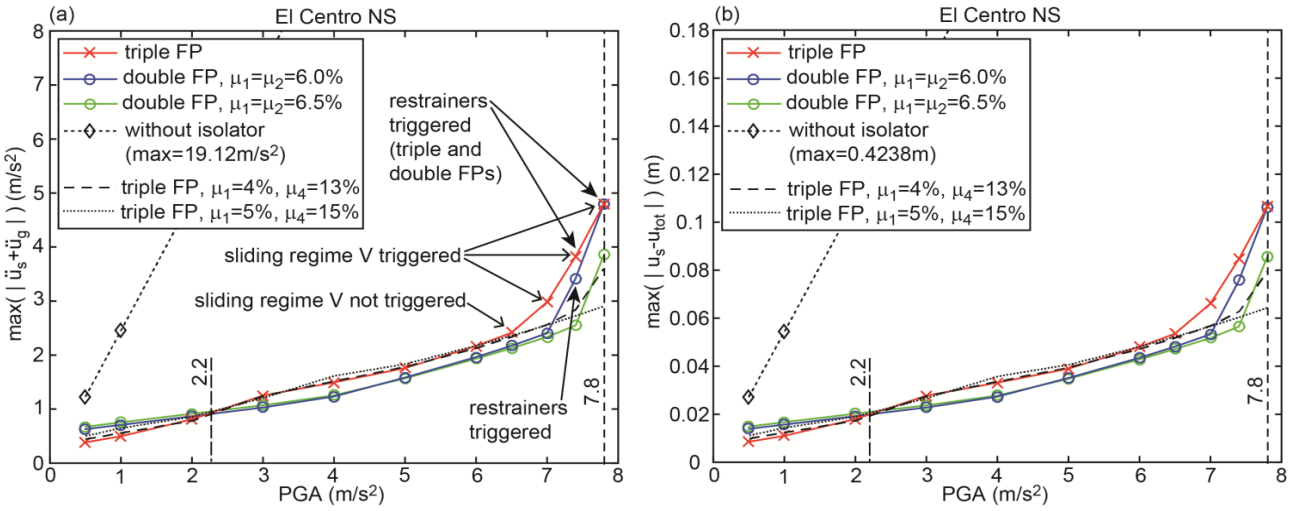

Figure 8. (a) Extreme of absolute acceleration of structure and (b) extreme of total drift of structure due to triple FP, double FP and without isolator due to El Centro NS earthquake

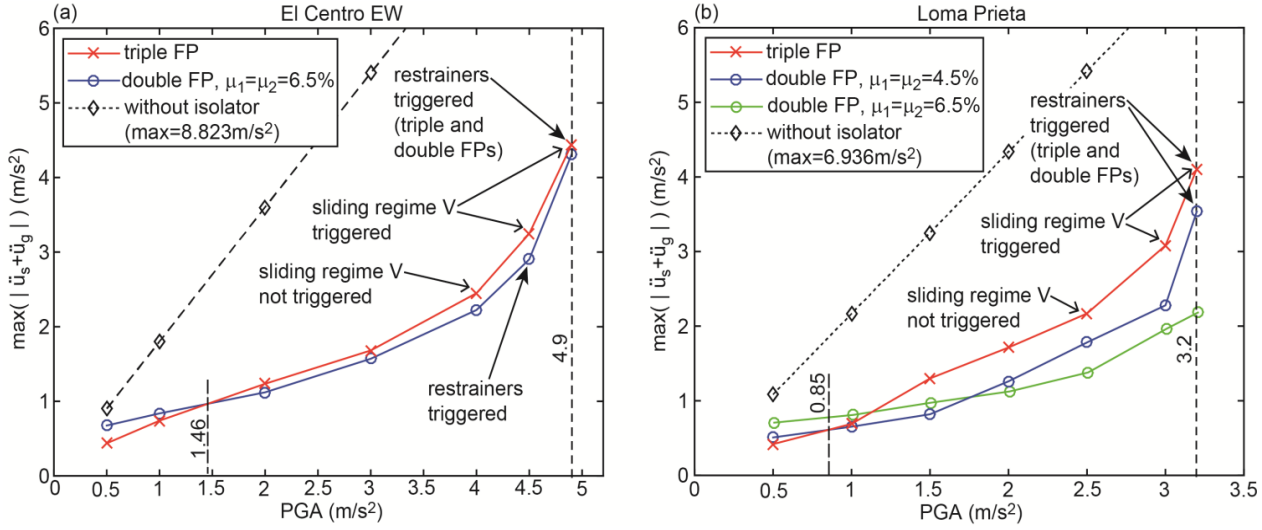

Figure 9. Extreme of absolute acceleration of structure due to triple FP, double FP and without isolator due to (a) El Centro EW and (b) Loma Prieta earthquakes

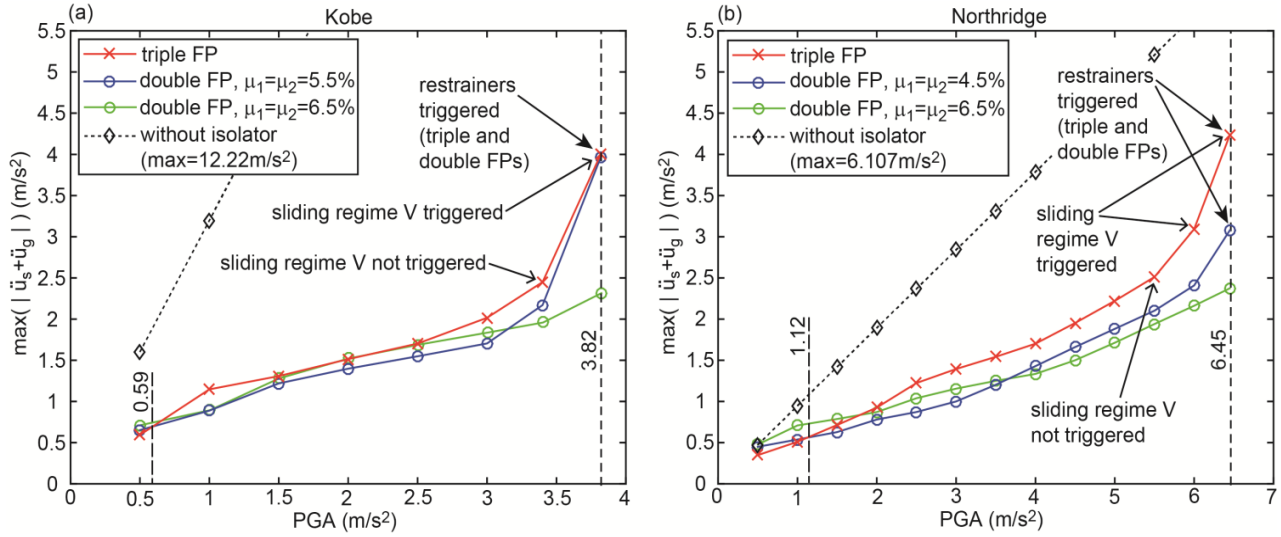

Figure 10. Extreme of absolute acceleration of structure due to triple FP, double FP and without isolator due to (a) Kobe and (b) Northridge earthquakes

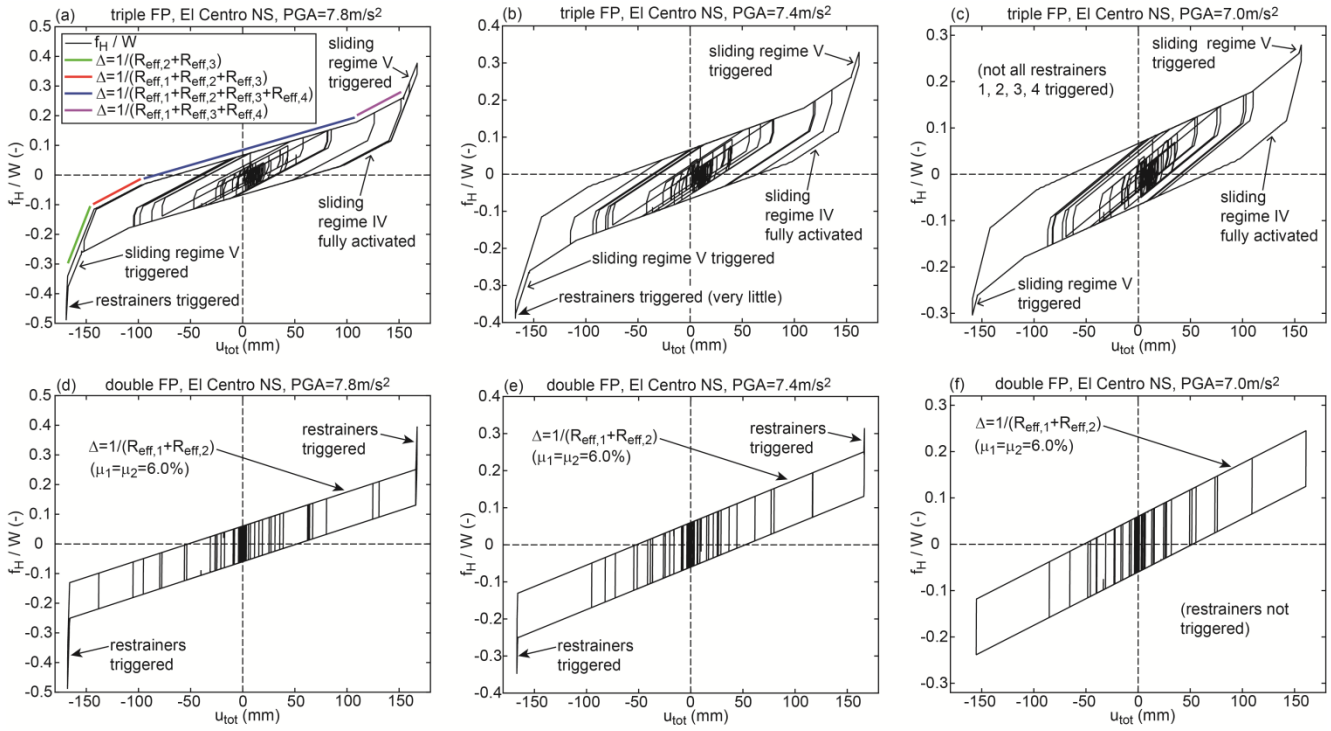

Figure 11. Horizontal force versus total displacement of triple FP due to El Centro NS for (a) PGA=7.8 m/s^2, (b) PGA=7.4 m/s^2, (c) PGA=7.0 m/s^2 and of double FP due to El Centro NS for (d) PGA=7.8 m/s^2, (e) PGA=7.4 m/s^2 and (f) PGA=7.0 m/s^2

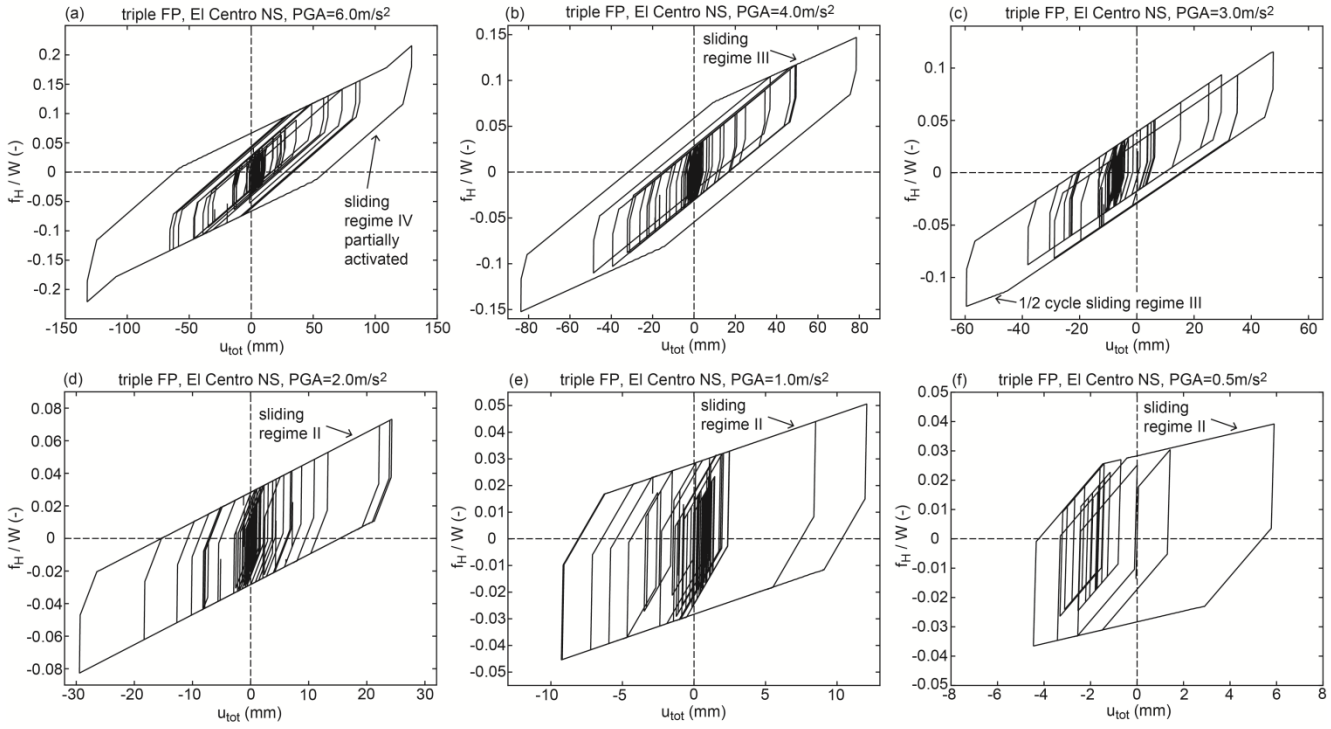

Figure 12. Horizontal force versus total displacement of triple FP due to El Centro NS for (a) PGA=6.0 m/s^2, (b) PGA=4.0 m/s^2, (c) PGA=3.0 m/s^2, (d) PGA=2.0 m/s^2, (e) PGA=1.0 m/s^2 and (f) PGA=0.5 m/s^2

5. Friction in Proportion to Displacement Amplitude

5.1. Adaptive Friction?

As demonstrated in section 2 the equivalent friction coefficient of the triple FP increases with increasing bearing relative motion within sliding regimes II to IV which primarily determine the dynamic behaviour of the triple FP (Figure 3(a)). Also within sliding regimes II to IV the equivalent stiffness coefficient shows a decreasing trend (Figure 3(b)). Both adaptive behaviours are commonly considered to improve the isolation of the primary structure. However, the results presented in section 4 demonstrate the contrary, i.e. the conventional non-adaptive double FP outperforms the triple FP at medium to higher shaking levels at which sliding regimes II to IV are activated.

In order to better understand how friction should depend on bearing motion in order to improve structural isolation a case study is performed where the friction coefficient of the pendulum is controlled in proportion to bearing displacement amplitude which is described subsequently.

5.2. Energy Balance with Linear Viscous Damper

The goal of any damping mechanism is to maximize the cycle energy of the damping device independent of its displacement amplitude. This means that the damping device should be linear, i.e. produce linear viscous damping. In order to obtain the control law of a controlled friction device it is therefore reasonable to balance the cycle energies of a linear viscous damper and a friction damper [47, 48]

$$\pi c(2\pi\, fr)U^2 = 4(\mu W)U \tag{17}$$

where c denotes the viscous damper coefficient of the linear viscous damper and harmonic excitation is assumed. Equation (17) can be interpreted as the cycle energy balance of a pendulum (without friction) with a linear viscous damper in parallel and a conventional FP. Solving (17) for the friction coefficient and omitting all constant variables yields

$$\mu \sim \frac{U}{fr} \tag{18}$$

Furthermore, $fr \approx const.$ may be assumed considering that the frequency fr of the relative motion of the FP is in the vicinity of the isolation frequency $fr_{isolation}$ that is given by the curvature (R_{eff}) of the FP. With this assumption it turns out that the **friction coefficient should be adjusted in proportion to relative displacement amplitude** [47-53]

$$\mu \sim U \tag{19}$$

5.3. Ideal Pendulum with Friction in Proportion to Displacement Amplitude

Ideally, a curved surface without any friction is combined with a controllable damper [54], e.g. a magnetorheological damper [27, 28, 55], to realize (19). The according real-time controlled friction force of the controllable damper becomes

$$f_{ideal} = sgn(\dot{u})\,\frac{\mu_1}{U_1} W U_{actual} \tag{20}$$

where μ_1 / U_1 denotes the gradient of friction relative to displacement amplitude (indicated by the dashed line in red in Figure 13(a)) and U_{actual} is the actual displacement amplitude. The resulting force displacement characteristics including the restoring stiffness force due to the curvature are depicted in Figure 13(a) for five selected U_{actual}.

5.4. Real Pendulum with Passive (Lubricated) Friction and Real-time Controlled Friction

In reality, friction of curved surfaces cannot be avoided. The lowest value is obtained when the sliding surface is lubricated. Typically, the lubricated (passive, uncontrollable) friction coefficient μ_0 is around 1%. The sum of the force due to lubricated friction of the FP and the controlled friction force of the controllable damper therefore becomes

$$f_{real} = sgn(\dot{u})\left\{\mu_0 W + \frac{(\mu_1 - \mu_0)}{U_1} W U_{previous}\right\} \tag{21}$$

Here, $U_{previous}$ denotes the previous (latest) displacement amplitude as the previous value is the latest value available in real-time control [50]. The resulting force displacement trajectories due to the simulation of the Loma Prieta earthquake scaled to PGA=2 m/s^2 show local loops (Figure 13(b)) due to the broad band excitation of the accelerogram in contrast to the force displacement trajectories shown in Figure 13(a) that result from kinematic excitation at constant frequency and constant amplitude.

5.5. Assessment for Two Accelerograms

The isolation performance of the pendulum with lubricated (passive, uncontrollable) friction and real-time controlled friction force according to (21) is computed for the accelerograms of the El Centro NS and the Loma Prieta earthquakes. The results plotted in Figures 14(a, b) are compared to those of two double FPs without restrainers to avoid the deteriorated isolation results at PGAs in the vicinity of PGA_{max} and to those of two triple FPs with increased friction coefficients also to avoid the worse isolation results when all restrainers are activated as seen in, e.g., Figures 8(a, b).

It is observed that the pendulum with lubricated (passive, uncontrollable) friction of 1% and a friction force that is adjusted in real-time in proportion to the previous displacement amplitude significantly outperforms all other computed double and triple FPs within the entire PGA range. The values of the absolute structural peak accelerations almost describe a straight line which means that **controlling the friction force in proportion to displacement**

amplitude linearizes the friction damper over each cycle (the force is still a friction force, see Figure 13(b)) which is the direct result of the energy balance with the linear viscous damper (17). A linear line would be obtained if μ_0 =0% and amplitude estimation errors were not present which corresponds to the ideal pendulum with controlled friction according to (20). It is also observed that the conventional double FP generates the same isolation as approach (21) at these PGAs for which the constant friction coefficients $\mu_1 = \mu_2$ of the conventional double FP are correctly tuned to the bearing displacement amplitude which is triggered when the peak of the structural acceleration occurs. The slightly better isolation result of the double FP with $\mu_1 = \mu_2$ =6.5% for the Loma Prieta accelerogram scaled to PGA=2.5 m/s^2 is caused by the fact that the friction coefficient of (21) is controlled in proportion to $U_{previous}$ which is not the actual amplitude whereby small real-time tuning errors in the actual friction force (21) are present.

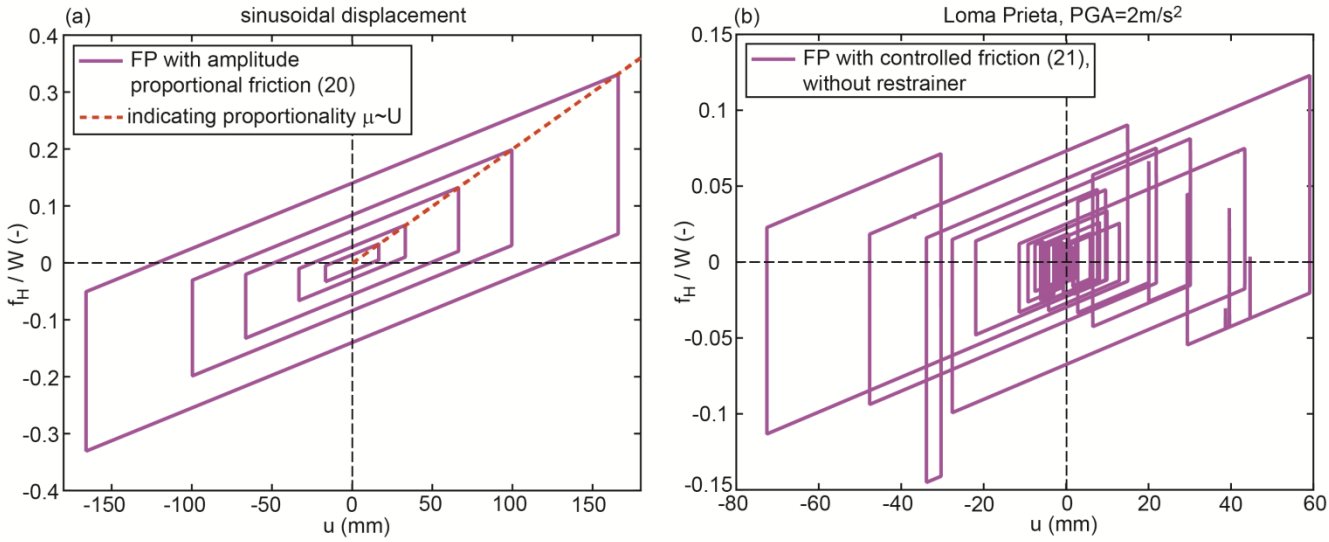

Figure 13. Force displacement trajectories of (a) FP according to (20) for kinematic excitation and (b) FP according to (21) due to ground excitation

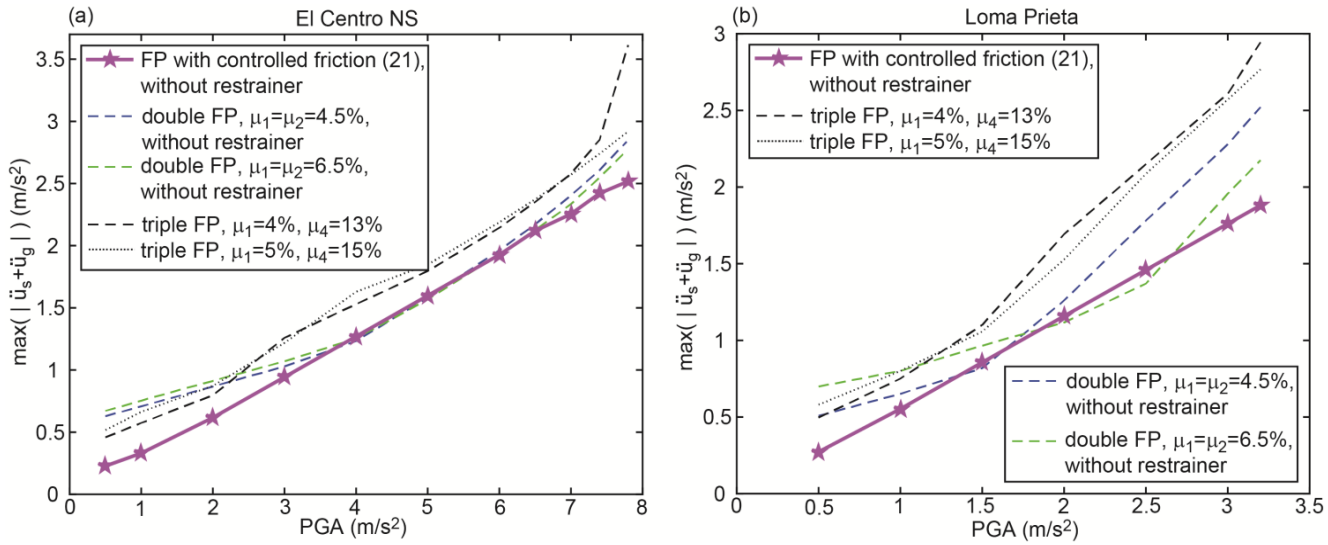

Figure 14. Performance of single FP with friction controlled in real-time in proportion to displacement amplitude for (a) El Centro NS and (b) Loma Prieta earthquakes compared with double FPs without restrainers and best performing triple FPs

6. Conclusions

The triple friction pendulum (FP) is well-known for its adaptive friction and stiffness properties that depend on its sliding regimes and bearing displacement amplitude, respectively, and consequently on peak ground acceleration (PGA) of the considered accelerogram. This paper therefore assesses the isolation performance in terms of absolute structural peak acceleration as function of various PGAs ranging between very small values up to the maximum value at which the full displacement capacity of the triple FP is used. The resulting isolation results demonstrate that the low friction of the articulated slider assembly is beneficial as it triggers relative motion in the bearing at small PGAs (<20% of its maximum) while the conventional non-adaptive double FP with same curvature outperforms the triple FP for all other PGAs. It is also observed that sliding regime V evokes a strongly deteriorated isolation due to the increased stiffness that reduces the isolation time period. In addition it is found that the increased stiffness of sliding regime V cannot reduce the displacement capacity of the triple FP because it is accompanied by reduced friction; the displacement capacity could be reduced by the combinations of increased stiffness and maintained friction or increased friction and maintained stiffness.

Based on the finding that the displacement (position) dependent friction of sliding regimes II to IV of the triple FP is not beneficial for enhanced structural isolation a pendulum is presented whose friction coefficient is controlled in proportion to bearing displacement amplitude. This approach is derived from the energy balance between linear viscous and friction dampers and requires the adoption of a controllable damper that works in parallel with the curved surface. To minimize the uncontrollable friction of the isolator the curved surface is assumed to be lubricated. The results demonstrate that the FP with friction controlled in proportion to displacement amplitude significantly enhances the isolation of the structure. Hence, displacement amplitude proportional friction is seen as the objective function for the future development of adaptive pendulums based on passive mechanisms without the adoption of control devices.

ACKNOWLEDGEMENTS

The authors gratefully acknowledge the financial support of MAURER SE, Munich, Germany.

REFERENCES

[1] R. I. Skinner, W. H. Robinson, and G. H. McVerry, An introduction to seismic isolation, Wiley: Chichester, England, 1993.

[2] A. K. Chopra, Dynamics of Structures: Theory and Applications to Earthquake Engineering, Prentice-Hall, 1995.

[3] F. Naeim, and J. M. Kelly, Design of Seismic Isolated Structures, Wiley: New York, 1999.

[4] C. A. Cornell, "Engineering Seismic Risk Analysis," Bulletin of the Seismological Society of America, vol. 58, pp. 1583–1606, 1968.

[5] M. Imbimbo, and J. M. Kelly, "Stability aspects of elastomeric isolators," Earthquake Spectra, vol. 13, issue 3, pp. 431–449, 1997.

[6] V. A. Zayas, S. S. Low, and S. A. Mahin, The FPS earthquake resisting system experimental report, Technical Report UBC/EERC-87/01, 1987.

[7] T. M. Al-Hussaini, V. A. Zayas, and M. C. Constantinou, Seismic isolation of multi-story frame structures using spherical sliding isolation systems, Technical Report NCEER-94-0007, 1994.

[8] C. S. Tsai, "Finite element formulations for friction pendulum seismic isolation bearings," International Journal for Numerical Methods in Engineering, vol. 40, pp. 29-49, 1997.

[9] K. Z. Y. Yen, and Y. J. Lee, Passive vibration isolating system, US Patent No. 6126136, October 3, 2000.

[10] D. M. Fenz, and M. C. Constantinou, "Behaviour of the double concave Friction Pendulum bearing," Earthquake Engng. Struct. Dyn., vol. 35, pp. 1403–1424, 2006.

[11] C. S. Tsai, W.-S. Chen, T.-C. Chiang, and B.-J. Chen, "Component and shaking table tests for full-scale multiple friction pendulum system," Earthquake Engng. Struct. Dyn., vol. 35, pp. 1653–1675, 2006.

[12] C. Bucher, "Probability-based optimization of friction damping devices," Structural Safety, vol. 31, pp. 500–507, 2009.

[13] R. Medeot, "Experimental validation of re-centring capability evaluation based on energy concepts," Proc. 14th World Conference on Earthquake Engineering, October 12-17, 2008, Beijing, China.

[14] C. Braun, "The sliding isolation pendulum – an improved recentring bridge bearing," Steel Construction, vol. 2, pp. 203–206, 2009.

[15] J. M. Kelly, "The role of damping in seismic isolation," Earthquake Engng. Struct. Dyn., vol. 28, issue 1, pp. 3–20, 1999.

[16] J. F. Hall, "Discussion of 'The role of damping in seismic isolation'," Earthquake Engng. Struct. Dyn., vol. 28, issue 12, pp. 1717–1720, 1999.

[17] Eurocode 8: Design of structures for earthquake resistance – Part 1: General rules, seismic actions and rules for buildings; EN 1998-1:2004 + AC: 2009.

[18] M. Q. Feng, M. Shinozuka, and S. Fujii, "Friction-controllable sliding isolation system," Journal of Engineering Mechanics (ASCE), vol. 119, issue 9, pp. 1845–1864, 1993.

[19] N. Wongprasert, and M. D. Symans, "Experimental evaluation of adaptive elastomeric base-isolated structures using variable-orifice fluid dampers," Journal of Structural Engineering (ASCE), vol. 131, issue 6, pp. 867–877, 2005.

[20] T. Kobori, M. Takahashi, T. Nasu, and N. Niwa, "Seismic response controlled structure with active variable stiffness

system," Earthquake Engng. Struct. Dyn., vol. 22, pp. 925–941, 1993.

[21] S. Nagarajaiah, and S. Sahasrabudhe, "Seismic response control of smart sliding isolated buildings using variable stiffness systems: An experimental and numerical study," Earthquake Engng. Struct. Dyn., vol. 35, issue 2, pp. 177–197, 2006.

[22] F. Casciati, L. Faravelli, and K. Hamdaoui, "Performance of a base isolator with shape memory alloy bars," Earthquake Engineering and Engineering Vibration, vol. 6, issue 4, pp. 401–408, 2007.

[23] N. Makris, "Rigidity–plasticity–viscosity: Can electrorheological dampers protect base isolated structures from near-source ground motions?," Earthquake Engng. Struct. Dyn., vol. 26, issue 5, pp. 571–591, 1997.

[24] J. C. Ramallo, E. A. Johnson, and B. F. Spencer Jr, "'Smart' base isolation systems," Journal of Engineering Mechanics (ASCE), vol. 128, issue 10, pp. 1088–1100, 2002.

[25] P. Y. Lin, P. N. Roschke, C. H. Loh, and C. P. Cheng, "Semi-active controlled base-isolation system with magnetorheological damper and pendulum system," Proceedings of the 13th World Conference on Earthquake Engineering, Vancouver, BC, Canada, 2004; Paper 691.

[26] H. Li, and J. Ou, "A design approach for semi-active and smart base-isolated buildings," Struct. Control Health Monit., vol. 13, issue 2–3, pp. 660–681, 2006.

[27] F. Weber, and M. Maślanka, "Precise Stiffness and Damping Emulation with MR Dampers and its Application to Semi-active Tuned Mass Dampers of Wolgograd Bridge," Smart Mater. Struct., vol. 23, 015019, 2014.

[28] F. Weber, "Robust force tracking control scheme for MR dampers," Struct. Control Health Monit., vol. 22, issue 12, pp. 1373–1395, 2015.

[29] A. Pocanschi, and M. C. Phocas, "Earthquake isolator with progressive nonlinear deformability," Engineering Structures, vol. 29, pp. 2586–2592, 2007.

[30] M. C. Constantinou, A. S. Whittaker, Y. Kalpakidis, D. M. Fenz, and G. P. Warn, Performance of seismic isolation hardware under service and seismic loading, Technical Report MCEER-07-0012, State University of New York at Buffalo, Buffalo, NY, 2007.

[31] D. M. Fenz, and M. C. Constantinou, "Spherical sliding isolation bearings with adaptive behavior: Theory," Earthquake Engng. Struct. Dyn., vol. 37, pp. 163–183, 2008.

[32] D. M. Fenz, and M. C. Constantinou, "Spherical sliding isolation bearings with adaptive behavior: Experimental verification," Earthquake Engng. Struct. Dyn., vol. 37, pp. 185–205, 2008.

[33] D. M. Fenz, and M. C. Constantinou, Development, Implementation and Verification of Dynamic Analysis Models for Multi-Spherical Sliding Bearings, Technical Report MCEER-08-0018, State University of New York at Buffalo, Buffalo, NY, 2008.

[34] M. C. Constantinou, and D. M. Fenz, Mechanical Behavior of Multi-spherical Sliding Bearings, MCEER-08-0007, 2008.

[35] D. M. Fenz, and M. C. Constantinou, "Modeling Triple Friction Pendulum Bearings for Response-History Analysis," Earthquake Spectra, vol. 24, issue 4, pp. 1011–1028, 2008.

[36] F. Fadi, and M. C. Constantinou, "Evaluation of simplified methods of analysis for structures with triple friction pendulum isolators," Earthquake Engng. Struct. Dyn., vol. 39, pp. 5–22, 2010.

[37] F. Hamidreza, and G. A. Gholamreza, "Nonlinear Response-History Analysis of Triple Friction Pendulum Bearings (TFPB), Installed Between stories Stories," Proc. 15th World Conf. Earthquake Engineering, Lisboa, 2012.

[38] T. A. Morgan, and S. A. Mahin, The Use of Base Isolation Systems to Achieve Complex Seismic Performance Objectives, PEER Report 2011/06, Pacific Earthquake Engineering Research Center, College of Engineering, University of California, Berkeley, July 2011.

[39] N. D. Dao, K. L. Ryan, E. Sato, and T. Sasaki, "Predicting the displacement of Triple Pendulum bearings in a full scale shaking experiment using a three-dimensional element," Earthquake Engng. Struct. Dyn., vol. 42, pp. 1677–1695, 2013.

[40] A. P. Giammona, K. L. Ryan, and N. D. Dao, "Evaluation of Assumptions Used in Engineering Practice to Model Buildings Isolated with Triple Pendulum Isolators in SAP2000," Earthquake Spectra, vol. 31, issue 2, pp. 637–660, 2015.

[41] C. Bucher, "Analysis and Design of Sliding Isolation Pendulum Systems," Proc. IABSE Conference Nara, May 13-15, 2015.

[42] L. Meirovitch, Fundamentals of Vibrations, New York: McGraw-Hill, 2001.

[43] F. Al-Bender, V. Lampaert, and J. Swevers, "The Generalized Maxwell-Slip Model: A Novel Model for Friction Simulation and Compensation," IEEE Transactions on Automatic Control, vol. 50, issue 11, pp. 1883–1887, 2005.

[44] M. Ruderman, "Presliding hysteresis damping of LuGre and Maxwell-slip friction models," Mechatronics, vol. 30, pp. 225–230, 2015.

[45] C. S. Tsai, T.-C. Chiang, and B.-J. Chen, "Experimental evaluation of piecewise exact solution for predicting seismic responses of spherical sliding type isolated structures," Earthquake Engng Struct. Dyn., vol. 34, pp. 1027–1046, 2005.

[46] P. M. Colvi, M. Moratti, and G. M. Celvi, "Seismic Isolation devices based on variable friction sliding materials," Proggettazione Sismico, vol. 6, issue 1, pp. 17–44, 2015.

[47] F. Weber, J. Høgsberg, and S. Krenk, "Optimal tuning of amplitude proportional Coulomb friction damper for maximum cable damping," Journal of Structural Engineering, vol. 136, issue 2, pp. 123–134, 2010.

[48] F. Weber, and C. Boston, "Energy Based Optimization of Viscous-Friction Dampers on Cables," Smart Mater. Struct., vol. 19, 045025, 2010.

[49] F. Weber, and C. Boston, "Clipped viscous damping with negative stiffness for semi-active cable damping," Smart Mater. Struct., vol. 20, 045007, 2011.

[50] F. Weber, and H. Distl, "Amplitude and frequency

independent cable damping of Sutong Bridge and Russky Bridge by MR dampers," Struct. Control Health Monit., vol. 22, pp. 237–254, 2015.

[51] F. Weber, and H. Distl, "Semi-active damping with negative stiffness for multi-mode cable vibration mitigation: Approximate collocated control solution," Smart Mater. Struct., vol. 24, 115015, 2015.

[52] F. Weber, "Semi-active vibration absorber based on real-time controlled MR damper," Mechanical Systems and Signal Processing, vol. 46, issue 2, pp. 272-288, 2014.

[53] F. Weber, H. Distl, S. Fischer, and C. Braun, "MR Damper Controlled Vibration Absorber for Enhanced Mitigation of Harmonic Vibrations," Actuators, vol. 5, 2016, doi: 10.3390/act5040027.

[54] M. A. Riley, A. M. Reinhorn, and S. Nagarajaiah, "Implementation issues and testing of a hybrid sliding isolation system," Engineering Structures, vol. 20, issue 3, pp. 144–154, 1998.

[55] F. Weber, H. Distl, and C. Braun, "Semi-active Base Isolation of Civil Engineering Structures Based on Optimal Viscous Damping and Zero Dynamic Stiffness," Proc. IMAC–XXXV Conference and Exposition on Structural Dynamics, January 30 – February 2, 2017, Garden Grove, CA, USA.